

A Non-uniform Time-stepping Convex Splitting Scheme for the Time-fractional Cahn-Hilliard Equation

Jun Zhang *

Jia Zhao †

JinRong Wang ‡

January 21, 2022

Abstract

In this paper, a non-uniform time-stepping convex-splitting numerical algorithm for solving the widely used time-fractional Cahn-Hilliard equation is introduced. The proposed numerical scheme employs the $L1^+$ formula for discretizing the time-fractional derivative and a second-order convex-splitting technique to deal with the non-linear term semi-implicitly. Then the pseudospectral method is utilized for spatial discretization. As a result, the fully discrete scheme has several advantages: second-order accurate in time, spectrally accurate in space, uniquely solvable, mass preserving, and unconditionally energy stable. Rigorous proofs are given, along with several numerical results to verify the theoretical results, and to show the accuracy and effectiveness of the proposed scheme. Also, some interesting phase separation dynamics of the time-fractional Cahn-Hilliard equation has been investigated.

1 Introduction

The Cahn-Hilliard (CH) equation was originally introduced to describe the process of coarsening dynamics of binary alloys. Ever since, a great deal of peer-reviewed papers have been published investigating different aspects of the Cahn-Hilliard equation [1–7], as well as applying it in many fields. For a mixture with two component, use ϕ to label the components: $\phi = 1$ to label one component, and $\phi = -1$ to label the other

*Computational Mathematics Research Center, Guizhou University of Finance and Economics, Guiyang, Guizhou 550025, China; Department of Mathematics, Guizhou University, Guiyang, Guizhou 550025, China; Email: jzhang@mail.gufe.edu.cn.

†Department of Mathematics and Statistics, Utah State University, Logan, UT, 84322, USA; Email: jia.zhao@usu.edu.

‡Department of Mathematics, Guizhou University, Guiyang, Guizhou 550025, China; School of Mathematical Sciences, Qufu Normal University, Qufu 273165, Shandong, China; Email: jrwang@gzu.edu.cn.

component. Then, the evolution dynamics could be modeled by the Cahn-Hilliard equation

$$\begin{cases} \partial_t \phi + M(-\Delta)(-\varepsilon^2 \Delta \phi + \phi^3 - \phi) = 0, & \mathbf{x} \in \Omega \subset R^d, \quad 0 < t \leq T, \\ \phi(\mathbf{x}, 0) = \phi_0(\mathbf{x}), \end{cases} \quad (1.1)$$

with proper physically relevant boundary conditions. Here Ω is the domain, $d = 2, 3$ is the spatial dimension, $M > 0$ is the mobility parameter and ε controls the length scale of transition regions. It could be shown that the equation (1.1) is a H^{-1} gradient flow with respect to the free energy

$$E(\phi) = \int_{\Omega} \left[\frac{\varepsilon^2}{2} |\nabla \phi|^2 + \frac{1}{4} (\phi^2 - 1)^2 \right] d\mathbf{x}. \quad (1.2)$$

Some well-known properties include: the total mass of each component is conserved, which could be easily verified by realizing

$$\int_{\Omega} \phi(\mathbf{x}, t) d\mathbf{x} = \int_{\Omega} \phi(\mathbf{x}, 0) d\mathbf{x};$$

and the free energy is non-increasing in time, which could be justified by noticing

$$\frac{dE}{dt} = \int_{\Omega} \frac{\delta E}{\delta \phi} \frac{\delta \phi}{\delta t} d\mathbf{x} = - \int_{\Omega} M \left| \nabla (-\varepsilon^2 \Delta \phi + \phi^3 - \phi) \right|^2 d\mathbf{x}, \quad (1.3)$$

given the boundary integral terms vanishes.

Nowadays, the Cahn-Hilliard model has emerged as a classical mathematical physics model in various applications. However, solving the Cahn-Hilliard equation is non-trivial, given the stiffness introduced by ε and the nonlinearity in the equation. Many generalized numerical algorithms have been developed to overcome such difficulties, which include the convex splitting method [8–10], the linear stabilization method [3, 11, 12], the Invariant Energy Quadratization (IEQ) approach [13], and the scalar auxiliary variable (SAV) method [14]. In addition, there have been extensive works of specific numerical schemes for the Cahn-Hilliard equation, such as second-order finite difference [15, 16], fourth-order finite difference scheme [5], pseudospectral scheme [17], and mixed finite element method [18, 19]. Moreover, many convex splitting schemes [10, 20–26] have been applied to various gradient flow models such as phase-field crystal equation, the modified phase field crystal equation, epitaxial thin film growth equation, nonlocal Cahn-Hilliard model, and coupled system of phase field equations.

To manipulate the coarsening dynamics, researchers have proposed some extensions of the classical Cahn-Hilliard equation. For instance, the viscous Cahn-Hilliard equation is postulated by introducing the inertia effect into the dissipation dynamics. One other option of introducing a memory effect (inertia) is to take advantage of the fractional time derivative. Thus, the time-fractional Cahn-Hilliard equation has been

introduced, which reads as

$$\begin{cases} \partial_t^\alpha \phi + M(-\Delta)(-\varepsilon^2 \Delta \phi + \phi^3 - \phi) = 0, & \mathbf{x} \in \Omega \subset \mathbb{R}^d, \quad 0 < t \leq T, \\ \phi(\mathbf{x}, 0) = \phi_0(\mathbf{x}), \end{cases} \quad (1.4)$$

where $d = 2, 3$, $\alpha \in (0, 1)$ is the time-fractional order, M is the mobility parameter, and ε is an artificial parameter controlling the interfacial thickness. Here $\partial_t^\alpha \phi$ denotes the classical Caputo derivative defined as

$$\partial_t^\alpha \phi(\mathbf{x}, t) = \frac{1}{\Gamma(1 - \alpha)} \int_0^t \frac{\partial \phi(\mathbf{x}, s)}{\partial s} \frac{ds}{(t - s)^\alpha}, \quad 0 < \alpha < 1. \quad (1.5)$$

The time-fractional models are known to maintain the memory effect of materials.

Though with its popularity, the time-fractional Cahn-Hilliard equation has not been derived physically, and its thermodynamic properties are not well understood. In particular, the classical gradient flow problem is known to be derived by energy variation, which makes the derived model satisfy the law of energy dissipation. Whether the fractional-order model also satisfy similar energy dissipation is still an open question. In the meanwhile, there are intensive research activities in understanding the time-fractional phase-field models or gradient flows, and their various anomalous coarsening dynamics in general. With many seminal work has been published, here we only emphasize some relevant research results. For a detailed reference list, please check the papers [27–33], and references therein. For the time-fractional phase-field model, Tang et al. [31] obtained an energy dissipation property with an integral type. They proved that the numerical method with the $L1$ formula for discretizing the fractional time derivative satisfies the energy dissipation property under suitable conditions [34]. In our previous work, we considered a series of time-fractional phase-field models, and show numerically that the time-fractional phase-field model follows a scaling law in the coarsening process [29, 32, 33]. Furthermore, we observed a linear proportional relationship between the decay rate of energy and fractional derivative α , which is in agreement with their counterparts (the integer phase-field models) [11, 35]. This is an exciting phenomenon by revealing the hidden connections between integer and fractional phase-field models. And it sheds light on how the scaling law is implemented. Liao et al. constructed a novel $L1^+$ formula coupled with IEQ/SAV method to approximate a time-fractional molecular beam epitaxial growth models [36] and the Allen-Cahn equation [37]. They proved that the numerical method is energy stable under a discrete integral summation.

For solving phase-field models, adaptivity in time is essential to save computational resources dramatically [38]. When the time mesh is uniform, Tang et al. [31] propose a stable time-discrete scheme using the classical $L1$ formula for the fractional time derivative. Their algorithm can't be applied to take into account the weak singularity of the initial state at $t = 0$, and it is not proper to assume that the solution is smooth in the entire closed domain. For non-smooth initial values, Jin et al. [39] prove that the $L1$ scheme could not

achieve $2 - \alpha$ order accuracy. Thus, when the time mesh is non-uniform, the $L1$ formula won't guarantee the energy stability anymore. The main goal of this work is to develop an efficient numerical scheme for the time-fractional Cahn-Hilliard model with non-uniform time steps, which can handle initial singularity and obeys the energy inequality, i.e., energy stable. Our numerical scheme is performed by utilizing a $L1^+$ formula [36] for time-fractional derivative and a convex splitting technique [20] for non-linear energy function. We show that our numerical method is uniquely solvable, unconditionally stable, and satisfies the property of energy dissipation. Several numerical examples are proposed to verify that the numerical scheme can achieve a second-order accuracy in the time direction. At last, the coarsening dynamics have been studied.

The rest of the article is organized as follows. In Section 2, we will briefly introduce the time-fractional Cahn-Hilliard equation. Then the $L1^+$ formula and the convex splitting scheme are studied in detail. Some properties of the newly proposed schemes will be introduced, along with detailed proofs. In Section 3, several numerical experiments are performed to demonstrate the effectiveness of the numerical methods. The conclusion of this article is given in the last section.

2 A Non-Uniform Time Stepping Numerical Algorithm

For better explanation, we first introduce some notations. Let (\cdot, \cdot) be the L^2 inner product. Define for $m \geq 0$

$$H^{-m}(\Omega) = (H^m(\Omega))^*, \quad H_0^{-m}(\Omega) = \{\varphi \in H^{-m}(\Omega) | (\varphi, 1)_m = 0\}, \quad (2.1)$$

here $(\varphi, 1)_m$ be the dual product between $H^m(\Omega)$ and $H^{-m}(\Omega)$. For $u \in L_0^2(\Omega)$, denote $-\Delta^{-1}u = \varphi \in H^1(\Omega) \cap L_0^2(\Omega)$, here φ be the solution of

$$-\Delta\varphi = u, \quad \text{in } \Omega, \quad (2.2)$$

$$(i) \varphi \text{ is periodic ; or } (ii) \frac{\partial\varphi}{\partial n} = 0, \quad \text{on } \partial\Omega. \quad (2.3)$$

Since the CH equation is an H^{-1} gradient flow, we define inner product and norm as

$$(f, (-\Delta)^{-1}g) = \left((-\Delta)^{-\frac{1}{2}}f, (-\Delta)^{-\frac{1}{2}}g \right), \quad \|f\|_{-1} := \|(-\Delta)^{-\frac{1}{2}}f\|. \quad (2.4)$$

2.1 Time-fractional Cahn-Hilliard equation

In this paper we focus on the time-fractional Cahn-Hilliard (TFCH) equation as follows

$$\begin{cases} \partial_t^\alpha \phi + M(-\Delta)(-\varepsilon^2 \Delta \phi + \phi^3 - \phi) = 0, & \mathbf{x} \in \Omega \quad 0 < t \leq T, \\ \phi(\mathbf{x}, 0) = \phi_0(\mathbf{x}), \end{cases} \quad (2.5)$$

with periodic boundary condition. Here we assume $\Omega \subset R^d$, is a smooth domain, with boundary $\partial\Omega$, and $d = 2, 3$. $\alpha \in (0, 1)$ is the time-fractional order, M is the mobility parameter, and ε is an artificial parameter controlling the interfacial thickness. Here $\partial_t^\alpha \phi$ denotes the classical Caputo derivative

$$\partial_t^\alpha \phi(\mathbf{x}, t) := \left(\mathcal{I}_t^{1-\alpha} \partial_t \phi(\mathbf{x}, t) \right)(t) = \frac{1}{\Gamma(1-\alpha)} \int_0^t \frac{\partial_s \phi(\mathbf{x}, s)}{(t-s)^\alpha} ds, \quad (2.6)$$

where $\mathcal{I}_t^\beta, \beta > 0$ is the Riemann-Liouville fractional integration operator defined as

$$(\mathcal{I}_t^\beta \phi)(t) = \int_0^t \frac{1}{\Gamma(\beta)} \frac{\phi(\mathbf{x}, s)}{t^{1-\beta}} ds, \quad (2.7)$$

and $\Gamma(\bullet)$ denotes the Γ -function.

For simplicity, in the rest of this paper, we will assume periodic boundary conditions for the time-fractional Cahn-Hilliard model (2.5). Notice the proposed scheme, along with its properties, also holds for homogeneous Neumann boundary conditions. It could be verified that the time-fractional Cahn-Hilliard model (2.5) has two essential properties.

Property 2.1 (Mass Conservation). *The time-fractional Cahn-Hilliard equation in (2.5) preserves the total mass, in the sense of*

$$\int_\Omega \phi(\mathbf{x}, t) d\mathbf{x} = \int_\Omega \phi(\mathbf{x}, 0) d\mathbf{x}. \quad (2.8)$$

Proof. We will verify (2.8) by showing that the solution of (2.5) satisfies

$$\frac{d}{dt} \int_\Omega \phi(\mathbf{x}, t) d\mathbf{x} = 0.$$

As a matter of fact, this could be verified by noticing

$$\begin{aligned} 0 &= \int_\Omega \partial_t^\alpha \phi(\mathbf{x}, t) d\mathbf{x} \\ &= \frac{1}{\Gamma(1-\alpha)} \int_\Omega \int_0^t \frac{\partial_t \phi(\mathbf{x}, s)}{(t-s)^\alpha} ds d\mathbf{x} \\ &= \frac{1}{\Gamma(1-\alpha)} \int_0^t \frac{1}{(t-s)^\alpha} \left[\int_\Omega \partial_t \phi(\mathbf{x}, s) d\mathbf{x} \right] ds, \end{aligned}$$

Since the domain Ω is independent of time, we obtain

$$\frac{d}{dt} \int_\Omega \phi(\mathbf{x}, t) d\mathbf{x} = \int_\Omega \partial_t \phi(\mathbf{x}, t) d\mathbf{x} = 0. \quad (2.9)$$

This completes the proof. □

Property 2.2 (Energy Bound). *It satisfies the following energy dissipation law*

$$E(\phi(\mathbf{x}, T)) - E(\phi(\mathbf{x}, 0)) = - \int_{\Omega} A_{\alpha}(\nabla \psi, \nabla \psi) d\mathbf{x} \leq 0, \quad \forall T \geq 0, \quad (2.10)$$

where

$$A_{\alpha}(f, g) = \frac{1}{\Gamma(1-\alpha)} \int_0^T \int_0^t \frac{f(s)g(s)}{(t-s)^{\alpha}} ds dt, \quad (2.11)$$

and $\psi = (-\Delta)^{-1}\phi_t$ is the solution of $-\Delta\psi = \phi_t$. Here, the effective free energy of (2.5) could be derived as

$$E(\phi) = \int_{\Omega} \left(\frac{\varepsilon^2}{2} |\nabla \phi|^2 + \frac{1}{4} (\phi^2 - 1)^2 \right) d\mathbf{x}. \quad (2.12)$$

The detailed proof for the property 2.2 could be found in [31]. We thus omit it for brevity.

2.2 Time discretization

In this section, we introduce the time discretization for the time-fractional Cahn-Hilliard model (2.5). We closely follow the notations in [36].

For given $T > 0$ and positive integer N , consider the non-uniform graded mesh $0 = t_0 < t_1 < \dots < t_n < \dots < t_N = T$, with time step $\tau_n = t_n - t_{n-1}$, $1 \leq n \leq N$. Given a sequence of grid functions $\{\phi^n\}_{n=1}^N$, define

$$\nabla_{\tau} \phi^n := \phi^n - \phi^{n-1}, \quad \partial_{\tau} \phi^{n-\frac{1}{2}} := \nabla_{\tau} \phi^n / \tau_n, \quad \phi^{n-\frac{1}{2}} := (\phi^n + \phi^{n-1})/2, \quad 1 \leq n \leq N. \quad (2.13)$$

Denote

$$\omega_{\alpha}(t) = \frac{1}{\Gamma(\alpha)} \frac{1}{t^{1-\alpha}}, \quad (2.14)$$

and let $\Pi_1 \phi(t)$ be the linear interpolant of $\phi(t)$ between t_{n-1} and t_n , that is

$$(\Pi_1 \phi)(t) := \partial_{\tau} \phi^{n-\frac{1}{2}}, \quad \forall t \in (t_{n-1}, t_n], \quad 1 \leq n \leq N. \quad (2.15)$$

Definition 2.1 ($L1$ Formula). The $L1$ formula for Caputo derivative is defined as

$$(\partial_{\tau}^{\alpha} \phi)^n := \int_{t_0}^{t_n} \omega_{1-\alpha}(t_n - s) \phi'(s) ds = \sum_{k=1}^n a_{n-k}^n \nabla_{\tau} \phi^k \quad (2.16)$$

where a_{n-k}^n 's are given as

$$a_{n-k}^n := \frac{1}{\tau_k} \int_{t_{k-1}}^{t_k} \omega_{1-\alpha}(t_n - s) ds, \quad 1 \leq k \leq n. \quad (2.17)$$

The $L1$ formula has several advantages. In particular, it could be easily seen that The coefficient a_{n-k}^n satisfies the following properties [40,41]

$$a_{n-k}^n > 0, \quad a_{n-k-1}^n \geq a_{n-k}^n, \quad 1 \leq k \leq n-1. \quad (2.18)$$

In particular, for uniform meshes, i.e., $t_n = \frac{n}{N}T$, we have

$$a_{n-k}^n = \frac{1}{\tau^\alpha} \left[\omega_{2-\alpha}(n-k+1) - \omega_{2-\alpha}(n-k) \right], \quad 1 \leq k \leq n. \quad (2.19)$$

The coefficients in (2.19) also satisfy the follow inequality.

Property 2.3 (Discrete Convolution Formula). *For any real sequence $\{\phi^i\}_{i=1}^n$, it holds*

$$\sum_{k=1}^n \sum_{j=1}^k a_{k-j}^n \phi^k \phi^j \geq 0. \quad (2.20)$$

The discrete convolution formula has been utilized in [31] to prove the energy dissipation property. However, it seems difficult to obtain similar semi-positive definite properties for non-uniform time grids. It turns out the $L1^+$ formula introduced in [36] will overcome such difficulties.

Definition 2.2 ($L1^+$ Formula (see [36])). The $L1^+$ formula of the Caputo derivative at $t^{n-\frac{1}{2}}$ is given as

$$\begin{aligned} (\partial_\tau^\alpha \phi)^{n-\frac{1}{2}} &:= \frac{1}{\tau_n} \int_{t_{n-1}}^{t_n} \int_0^t \omega_{1-\alpha}(t-s) (\Pi_1 \phi)'(s) ds dt \\ &= \sum_{k=1}^n \bar{a}_{n-k}^n \nabla_\tau \phi^k, \quad n \geq 1, \end{aligned} \quad (2.21)$$

where \bar{a}_{n-k}^n are defined by

$$\bar{a}_{n-k}^n := \frac{1}{\tau_k \tau_n} \int_{t_{n-1}}^{t_n} \int_{t_{k-1}}^{\min\{t, t_k\}} \omega_{1-\alpha}(t-s) ds dt, \quad 1 \leq k \leq n. \quad (2.22)$$

Obviously, the discrete convolution kernels \bar{a}_{n-k}^n is positive. In fact, they have many good properties. See [36] for details. Here we only emphasis the following one.

Property 2.4 (Discrete Convolution Formula). *For any real sequence $\{\phi^i\}_{i=1}^n$, it holds*

$$\sum_{k=1}^n \sum_{j=1}^k \bar{a}_{k-j}^k \phi^k \phi^j \geq 0. \quad (2.23)$$

For the nonlinear terms, we utilize a convex splitting strategy [20] to introduce an explicit-implicit temporal discretization. Overall, the semi-discrete scheme in time is proposed as

Scheme 2.1 (Non-uniform time marching scheme). Set $\phi^{-1} = \phi^0$. For given $T > 0$ and positive integer N , consider the non-uniform graded mesh $0 = t_0 < t_1 < \dots < t_m < \dots < t_N = T$, with time step $\tau_m = t_m - t_{m-1}$, $1 \leq m \leq N$. After we obtain ϕ^i , $i \leq n-1$ with $n \geq 1$, we can get ϕ^n via the following scheme

$$\begin{cases} (\partial_\tau^\alpha \phi)^{n-\frac{1}{2}} = M \Delta \mu^{n-\frac{1}{2}}, \\ \mu^{n-\frac{1}{2}} = -\frac{\varepsilon^2}{2} \left(\Delta \phi^{n-1} + \Delta \phi^n \right) + \frac{1}{4} \left((\phi^{n-1} + \phi^n) ((\phi^n)^2 + (\phi^{n-1})^2) \right) - \left(\frac{3}{2} \phi^{n-1} - \frac{1}{2} \phi^{n-2} \right), \end{cases} \quad (2.24)$$

where the formula for the temporal fractional derivative is given in (2.21).

Remark 2.1. It is worth mentioning that the above time-discrete scheme (2.24) works for any non-uniform grid. Therefore, the solution singularity near the initial time can be effectively handled by proposing proper non-uniform time meshes or smaller meshes in general. Also, in a certain time regime when dynamics evolve slow, larger time steps could be used to reduce the computational time significantly. Note that, by using $\phi^{-1} = \phi^0$, the local truncation error for the initial step is second-order, which implies that the overall method is globally second-order accurate in time. Meanwhile, numerical tests will verify that the time-discrete scheme can achieve second-order accuracy for certain examples.

The numerical scheme (2.24) and the full discrete scheme (2.42) are second-order accurate for ϕ^n when $\tau_n = \tau_{n-1}$, and first-order accurate for ϕ^n when $\tau_n \neq \tau_{n-1}$. As an improvement, we can easily achieve the second-order accuracy of the non-uniform time marching scheme by replacing $-(\frac{3}{2}\phi^{n-1} - \frac{1}{2}\phi^{n-2})$ with $-(\phi^{n-1} + \nabla_\tau \phi^{n-1}/2\rho_{n-1})$ in equation (2.24). Therefore, the improved scheme reads as below.

Scheme 2.1 (Non-uniform time marching scheme). Set $\phi^{-1} = \phi^0$. For given $T > 0$ and positive integer N , consider the non-uniform graded mesh $0 = t_0 < t_1 < \dots < t_m < \dots < t_N = T$, with time step $\tau_m = t_m - t_{m-1}$, $1 \leq m \leq N$. After we obtain ϕ^i , $i \leq n-1$ with $n \geq 1$, we can get ϕ^n via the following scheme

$$\begin{cases} (\partial_\tau^\alpha \phi)^{n-\frac{1}{2}} = M \Delta \mu^{n-\frac{1}{2}}, \\ \mu^{n-\frac{1}{2}} = -\frac{\varepsilon^2}{2} \left(\Delta \phi^{n-1} + \Delta \phi^n \right) + \frac{1}{4} \left((\phi^{n-1} + \phi^n) ((\phi^n)^2 + (\phi^{n-1})^2) \right) - (\phi^{n-1} + \nabla_\tau \phi^{n-1}/2\rho_{n-1}), \end{cases} \quad (2.24)$$

where the formula for the temporal fractional derivative is given in (2.21). Here the local time-step ratio $\rho_n := \tau_n/\tau_{n+1}$.

It is worth noting that such changes will not affect the subsequent proofs. The only difference for the proof of energy stability is an introduction of the time step ratio ρ_{n-1} restriction, that is $\rho_{n-1} \geq 0.5$, i.e. $\frac{\tau_n}{\tau_{n-1}} \leq 2$. And the only difference in the proof of the energy stability is in (2.38).

As a matter of fact, taking the inner product of the second equation in the scheme with $\nabla_\tau \phi^n$, we obtain

$$(\mu^{n-\frac{1}{2}}, \nabla_\tau \phi^n) = \frac{\varepsilon^2}{2} (\|\nabla \phi^n\|^2 - \|\nabla \phi^{n-1}\|^2) + \frac{1}{4} (\|\phi^n\|^4 - \|\phi^{n-1}\|^4) - \left(\phi^{n-1} + \nabla_\tau \phi^{n-1} / 2\rho_{n-1}, \nabla_\tau \phi^n \right).$$

We denote $\frac{1}{\rho_{n-1}} = 1 + a$, and use the following two identities

$$\begin{aligned} 2a(a-b) &= a^2 - b^2 + (a-b)^2, \\ 2(a-b)(b-c) &= (a-b)^2 + (b-c)^2 - (a-2b+c)^2. \end{aligned}$$

Given $\rho_{n-1} \geq \frac{1}{2}$, we have $|a| \leq 1$. Notice the fact

$$-\left(\phi^{n-1} + \nabla_\tau \phi^{n-1} / 2\rho_{n-1}, \nabla_\tau \phi^n \right) = -\left(\left(1 + \frac{1}{2\rho_{n-1}}\right) \phi^{n-1} - \frac{1}{2\rho_{n-1}} \phi^{n-2}, \phi^n - \phi^{n-1} \right).$$

We can find

$$\begin{aligned} & -\left(\phi^{n-1} + \nabla_\tau \phi^{n-1} / 2\rho_{n-1}, \nabla_\tau \phi^n \right) \\ &= -\left(\left(\frac{3}{2} + a\right) \phi^{n-1} - \left(\frac{1}{2} + a\right) \phi^{n-2}, \phi^n - \phi^{n-1} \right) \\ &= -\left(\frac{3}{2} \phi^{n-1} - \frac{1}{2} \phi^{n-2}, \phi^n - \phi^{n-1} \right) - a \left(\phi^{n-1} - \phi^{n-2}, \phi^n - \phi^{n-1} \right) \\ &= \frac{1}{2} \left[\|\phi^{n-1}\|^2 - \|\phi^n\|^2 + \frac{1}{2} \|\phi^n - \phi^{n-1}\|^2 \right] \\ &\quad - \frac{1}{4} \left[\|\phi^n - \phi^{n-1}\|^2 + \|\phi^{n-1} - \phi^{n-2}\|^2 - \|\phi^n - 2\phi^{n-1} + \phi^{n-2}\|^2 \right] - a \left(\phi^{n-1} - \phi^{n-2}, \phi^n - \phi^{n-1} \right) \\ &\geq \frac{1}{2} \|\phi^{n-1}\|^2 - \frac{1}{2} \|\phi^n\|^2 + \frac{1}{4} \|\phi^n - \phi^{n-1}\|^2 - \frac{1}{4} \|\phi^{n-1} - \phi^{n-2}\|^2 \\ &\quad + \frac{1}{4} \|\phi^n - 2\phi^{n-1} + \phi^{n-2}\|^2 - \frac{|a|}{4} \|\phi^n - 2\phi^{n-1} + \phi^{n-2}\|^2 \\ &\geq -\frac{1}{2} \|\phi^n\|^2 + \frac{1}{2} \|\phi^{n-1}\|^2 + \frac{1}{4} \|\phi^n - \phi^{n-1}\|^2 - \frac{1}{4} \|\phi^{n-1} - \phi^{n-2}\|^2. \end{aligned}$$

2.3 Properties of the semi-discrete scheme

For the proposed scheme (2.24), it satisfies several properties. First of all, it could be verified that

Theorem 2.1 (Existence and Uniqueness). *There exists a unique solution at each time step for the proposed scheme in (2.24).*

Proof. The proof is based on a convexity argument. In fact, we define the minimization problem

$$\min_{\phi} G(\phi), \tag{2.25}$$

where

$$G(\phi) = \frac{1}{4}(-\varepsilon \Delta \phi, \phi)_{L^2(\Omega)}^2 + (h_1(\phi), 1)_{L^2(\Omega)}^2 + (h_2(\phi), 1)_{H^{-1}(\Omega)}^2, \quad (2.26)$$

with $h_1(\phi)$ and $h_2(\phi)$ defined as

$$\begin{aligned} h_1(\phi) &= \frac{\phi^4}{4} + \frac{\phi^3}{3} \phi^{n-1} + \frac{\phi^2}{2} (\phi^{n-1})^2 + \phi (\phi^{n-1})^3 - \phi \left(\frac{\varepsilon^2}{2} \Delta \phi^{n-1} + \frac{3}{2} \phi^{n-1} - \frac{1}{2} \phi^{n-2} \right), \\ h_2(\phi) &= \frac{1}{2} \bar{a}_0^n \phi^2 + \left(\sum_{k=2}^n \bar{a}_{n-k}^n \nabla_\tau \phi^k - \bar{a}_0^n \phi^{n-1} \right) \phi. \end{aligned} \quad (2.27)$$

It could be easily verified that the target functional $G(\phi)$ is convex with respect to ϕ [20]. Then, there is a unique solution for (2.25).

Notice the solution to (2.24) is equivalent to the solution minimizing the convex functional. Thus, there exists a unique solution for (2.24). \square

Theorem 2.2 (Mass Conservation). *The time-discrete scheme (2.24) preserves the total mass, i.e.*

$$\int_{\Omega} \phi^n d\mathbf{x} = \int_{\Omega} \phi^0 d\mathbf{x}, \quad \forall n \geq 1. \quad (2.28)$$

Proof. This could be proved by induction by following the similar idea as in [37]. First of all, it could be easily shown $\int_{\Omega} \phi^1 d\mathbf{x} = \int_{\Omega} \phi^0 d\mathbf{x}$. Then, using the induction, assuming it holds $\int_{\Omega} \phi^k d\mathbf{x} = \int_{\Omega} \phi^0 d\mathbf{x}$, $\forall k < n$, we have

$$(\bar{a}_0^n \nabla_\tau \phi^n, 1) = ((\partial_\tau^\alpha \phi)^{n-\frac{1}{2}}, 1) = (M \nabla \mu^{n-\frac{1}{2}}, 1) = 0, \quad (2.29)$$

i.e.

$$\int_{\Omega} \phi^n d\mathbf{x} = \int_{\Omega} \phi^{n-1} d\mathbf{x} = \int_{\Omega} \phi^0 d\mathbf{x}. \quad (2.30)$$

Thus, the scheme (2.24) conserves the total mass. It completes the proof. \square

Theorem 2.3 (Energy Stability). *The time-discrete scheme (2.24) is unconditionally energy stable, and it follows the energy dissipation law as*

$$E(\phi^n) \leq E(\phi^0), \quad 1 \leq n \leq N. \quad (2.31)$$

Proof. From [42, 43], we know the weakly singular kernel $\omega_{1-\alpha}$ is positive semi-definite, that is

$$\begin{aligned} \mathcal{I}_t^1(w \mathcal{I}_t^{1-\alpha} w)(t) &= \int_0^t w(\eta) d\eta \int_0^\eta \omega_{1-\alpha}(\eta-s) w(s) ds \\ &= \frac{1}{2} \int_0^t \int_0^t \omega_{1-\alpha}(|\eta-s|) w(s) w(\eta) d\eta ds \\ &\geq 0. \end{aligned} \quad (2.32)$$

Taking $w = \Pi_1 \phi$ in (2.32), we know the the non-uniform $L1^+$ formula

$$(\partial_\tau^\alpha \phi)^{n-\frac{1}{2}} \approx \frac{1}{\tau_n} \int_{t_{n-1}}^{t_n} (\partial_t^\alpha \phi)(t) dt. \quad (2.33)$$

can ensure that the discrete convolution satisfies semi-positive characterization

$$\begin{aligned} \sum_{k=1}^n \nabla_\tau \phi^k (\partial_\tau^\alpha \phi)^{k-\frac{1}{2}} &= \int_{t_0}^t (\Pi_1 \phi)'(t) \int_0^t \omega_{1-\alpha}(t-s) (\Pi_1 \phi)'(s) ds dt \\ &= \mathcal{I}_t^1 \left((\Pi_1 \phi)' \mathcal{I}_t^{1-\alpha} (\Pi_1 \phi)' \right) (t_n) \\ &\geq 0. \end{aligned} \quad (2.34)$$

Combining with (2.22) and (2.34), for any real grid function $\{w_k\}_{k=1}^n$, we find

$$\sum_{k=1}^n w_k \sum_{j=1}^k \bar{a}_{n-k}^n w_j \geq 0. \quad (2.35)$$

Taking the inner product of first equation in (2.24) with $-\Delta^{-1} \nabla_\tau \phi^n$, we obtain

$$\left((\partial_\tau^\alpha \phi)^{n-\frac{1}{2}}, (-\Delta)^{-1} \nabla_\tau \phi^n \right) = -(\mu^{n-\frac{1}{2}}, \nabla_\tau \phi^n). \quad (2.36)$$

Taking the inner product of second equation in (2.24) with $\nabla_\tau \phi^n$, we obtain

$$(\mu^{n-\frac{1}{2}}, \nabla_\tau \phi^n) = \frac{\varepsilon^2}{2} (\|\nabla \phi^n\|^2 - \|\nabla \phi^{n-1}\|^2) + \frac{1}{4} (\|\phi^n\|^4 - \|\phi^{n-1}\|^4) - \left(\frac{3}{2} \phi^{n-1} - \frac{1}{2} \phi^{n-2}, \nabla_\tau \phi^n \right). \quad (2.37)$$

Notice the fact

$$\begin{aligned} & -\left(\frac{3}{2} \phi^{n-1} - \frac{1}{2} \phi^{n-2}, \nabla_\tau \phi^n \right) \\ &= -\frac{1}{2} \|\phi^n\|^2 + \frac{1}{2} \|\phi^{n-1}\|^2 + \frac{1}{2} \|\phi^n - \phi^{n-1}\|^2 - \frac{1}{2} (\phi^n - \phi^{n-1}, \phi^{n-1} - \phi^{n-2}) \\ &\geq -\frac{1}{2} \|\phi^n\|^2 + \frac{1}{2} \|\phi^{n-1}\|^2 + \frac{1}{2} \|\phi^n - \phi^{n-1}\|^2 - \frac{1}{4} \|\phi^n - \phi^{n-1}\|^2 - \frac{1}{4} \|\phi^{n-1} - \phi^{n-2}\|^2 \\ &= -\frac{1}{2} \|\phi^n\|^2 + \frac{1}{2} \|\phi^{n-1}\|^2 + \frac{1}{4} \|\phi^n - \phi^{n-1}\|^2 - \frac{1}{4} \|\phi^{n-1} - \phi^{n-2}\|^2. \end{aligned} \quad (2.38)$$

Summing the above equations up, we obtain

$$E(\phi^k) - E(\phi^{k-1}) \leq -\left((-\Delta)^{-\frac{1}{2}} (\partial_\tau^\alpha \phi)^{k-\frac{1}{2}}, (-\Delta)^{-\frac{1}{2}} \nabla_\tau \phi^k \right) - \frac{1}{4} \|\phi^k - \phi^{k-1}\|^2 + \frac{1}{4} \|\phi^{k-1} - \phi^{k-2}\|^2, \quad (2.39)$$

for any $2 \leq k \leq n$. Using the fact $\phi^0 = \phi^{-1}$, we have

$$E(\phi^1) - E(\phi^0) \leq -\left((-\Delta)^{-\frac{1}{2}} (\partial_\tau^\alpha \phi)^{\frac{1}{2}}, (-\Delta)^{-\frac{1}{2}} \nabla_\tau \phi^1 \right) - \frac{1}{4} \|\phi^1 - \phi^0\|^2. \quad (2.40)$$

By summing up for $k = 1, \dots, n$, and applying (2.32), we have

$$\begin{aligned} E(\phi^n) - E(\phi^0) &\leq - \int_{\Omega} \mathcal{I}_t^1 \left[((-\Delta)^{-\frac{1}{2}} \Pi_1 \phi)' \mathcal{I}_t^{1-\alpha} ((-\Delta)^{-\frac{1}{2}} \Pi_1 \phi)' \right] (t^n) d\mathbf{x} - \frac{1}{4} \|\phi^n - \phi^{n-1}\|^2 \\ &\leq 0. \end{aligned} \quad (2.41)$$

It completes the proof. \square

Remark 2.2. We obtained an energy stable numerical scheme for the time-fractional Cahn-Hilliard model. However, how to prove $E(\phi^n) \leq E(\phi^{n-1})$ for time-fractional gradient flow problem is still an open question. In addition, the error analysis of the numerical scheme is meaningful and challenging work.

2.4 Spatial discretization

For the spatial discretization, we use the Fourier Pseudo-spectral method. To make this paper self-consistent, we introduce a few notations. For more details, interested readers can refer to our previous work [44, 45].

Consider a rectangular domain $\Omega = [0, L_x] \times [0, L_y]$ with L_x and L_y the lengths of each sides. We partition the domain with uniform meshes, with mesh size $h_x = L_x/N_x, h_y = L_y/N_y$, where N_x and N_y be two positive even integers. Thus, the discrete domain is denoted as

$$\Omega_h = \{(x_j, y_k) | x_j = jh_x, y_k = kh_y, 0 \leq j \leq N_x - 1, 0 \leq k \leq N_y - 1\}.$$

Also, we introduce $V_h = \{u | u = \{u_{j,k} | (x_j, y_k) \in \Omega_h\}\}$ as the space of grid functions on Ω_h .

In order to derive the algorithm conveniently, we denote discrete gradient operator and the discrete Laplace operator as ∇_h and Δ_h . Applying the Fourier pseudospectral method in space to the semi-discrete scheme (2.24), we obtain the following fully discrete scheme

Scheme 2.2 (Full Discrete Scheme). Give the initial condition $\phi^0 = \phi_0 \in V_h$. Set $\phi^{-1} = \phi^0$. After we obtained $\phi^i, i \leq n-1$, with $n \geq 1$, we can update $\phi^n \in V_h$ via

$$\begin{cases} (\partial_\tau^\alpha \phi)^{n-\frac{1}{2}} = M \Delta_h \mu^{n-\frac{1}{2}}, \\ \mu^{n-\frac{1}{2}} = -\frac{\varepsilon^2}{2} (\Delta_h \phi^{n-1} + \Delta_h \phi^n) + \frac{1}{4} ((\phi^{n-1} + \phi^n)((\phi^n)^2 + (\phi^{n-1})^2)) - (\frac{3}{2} \phi^{n-1} - \frac{1}{2} \phi^{n-2}), \end{cases} \quad (2.42)$$

where the formula for the temporal fractional derivative is given in (2.21).

Here we emphasize that the fully discrete scheme also satisfies the three properties: solution existence and uniqueness, mass conservation, and energy dissipation in the full discrete sense. We omit the details as the proofs for the fully discrete scheme are similar to those for the semi-discrete scheme.

3 Numerical examples

In this section, the fully discrete numerical scheme in (2.42) is implemented. Then, we conduct a time-step refinement test to show the second-order temporal accuracy of the proposed scheme. Afterward, several numerical examples are shown to investigate the effects of fractional order α and initial profiles on phase separation dynamics.

3.1 Convergence tests

First of all, we perform a time convergence test to demonstrate its order of accuracy. Here we choose the domain $\Omega = [0, 1]^2$, and the parameters $\varepsilon = 0.01$, $M = 10 \times 10^{-5}$. We use 128^2 meshes, and choose the initial profile for ϕ as

$$\phi(x, y, t = 0) = \tanh \left(\frac{1}{\sqrt{2}\varepsilon} [\sqrt{(x - x_0)^2 + (y - y_0)^2} - 0.25 - \frac{1 + \cos(4 \arctan \frac{y - y_0}{x - x_0})}{16}] \right), \quad (3.1)$$

with $x_0 = y_0 = 0.5$. For different fractional order α , the numerical solution at $T = 0.01$ using different time steps $\Delta t = \frac{103}{2^n}$, $n \in \mathbb{N}$ are calculated. Since there is generally hard to find the exact solution, we define the reference 'exact' solution ϕ_{ij}^{ref} by the result with its nearest finer time step. the discrete l^2 norm of numerical errors $e_{ij} := \phi_{ij} - \phi_{ij}^{ref}$ are summarized in Table 3.1. It is observed that 2nd order accuracy in time is reached for the testing problem.

Table 3.1: The l^2 norm of numerical errors for ϕ at time $T = 0.01$ for time fractional Cahn-Hilliard equation with various fractional order α . They are computed by the proposed scheme in (2.42) using various temporal step sizes.

δt	L^2 Error ($\alpha = 0.8$)	Order	L^2 Error ($\alpha = 0.5$)	Order	L^2 Error ($\alpha = 0.35$)	Order
0.001	7.096×10^{-6}		4.357×10^{-5}		1.227×10^{-4}	
0.0005	1.854×10^{-6}	1.94	1.094×10^{-5}	1.99	1.603×10^{-5}	2.94
0.00025	4.811×10^{-7}	1.95	2.725×10^{-6}	2.01	3.970×10^{-6}	2.01
0.000125	1.241×10^{-7}	1.96	6795×10^{-7}	2.00	9.897×10^{-7}	2.00
0.0000625	3.186×10^{-8}	1.97	1.696×10^{-7}	2.00	2.472×10^{-7}	2.00
0.00003125	8.146×10^{-9}	1.97	4.234×10^{-8}	2.00	6.186×10^{-8}	1.99

3.2 Coarsening dynamics with various fractional order α

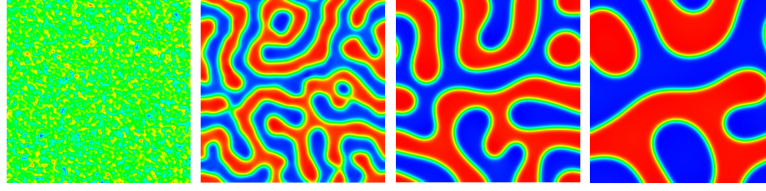
Next, we study the coarsening dynamics of the time-fractional Cahn-Hilliard equation with the newly proposed scheme. In this case, we choose the domain $\Omega = [0, 1]^2$, parameters $\varepsilon = 0.01$, $M = 0.1$. And we use 128^2 meshes. For this case, we use a randomly generated initial condition for ϕ as

$$\phi(x, y, t = 0) = 10^{-3} \text{rand}(x, y), \quad (3.2)$$

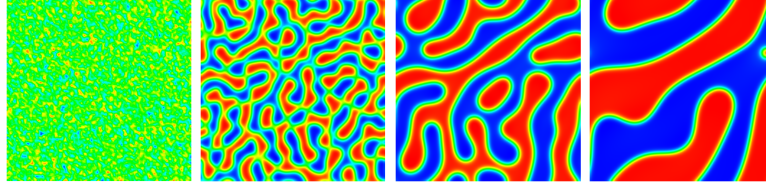
with $\text{rand}(x, y) \in [-1, 1]$ random numbers with uniform distribution. To reduce computational time without losing accuracy, we use an adaptive time marching strategy. Defining $\Delta t_{\min} = 10^{-4}$, $\Delta t_{\max} = 10^{-1}$ and $\beta = 10^7$, the time step Δt_{n+1} is chosen by following the formula

$$\Delta t_{n+1} = \begin{cases} \Delta t_{\min}, & n < K, \\ \max(\Delta t_{\min}, \frac{\Delta t_{\max}}{\sqrt{1+\beta \left| \frac{E^n - E^{n-1}}{\Delta t_n} \right|^2}}), & n \geq K, \end{cases} \quad (3.3)$$

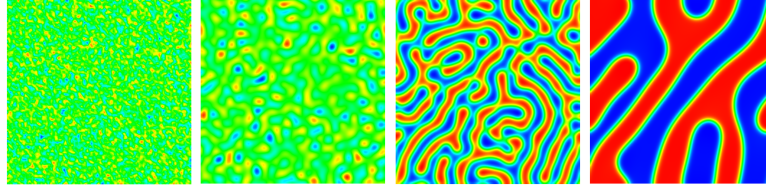
Here we pick $K = 100$. The profiles of ϕ at different times are summarized in Figure 3.1. We observe either case has similar coarsening dynamics. From the numerical simulations in 3.1, we also observe that the coarsening dynamics with smaller fractional-order α is faster than that with bigger fractional-order α in the time range $[0, 1]$.



(a) $\alpha = 0.35$



(b) $\alpha = 0.5$



(c) $\alpha = 0.8$

Figure 3.1: Comparison of coarsening dynamics with different fractional order α . Here we choose $\alpha = 0.35, 0.5, 0.8$ respectively. The profile of ϕ at approximately $t = 0, 0.001, 0.2, 1$ are plotted.

To further verify this, their corresponding energy evolution with time is shown in Figure 3.2, where we observe the energy with smaller fractional derivative α evolves faster. Also, we observe the energies in all cases (with different time-fractional derivative α) decrease with time. Notice in both the continuous theorem (2.10) and the discrete theorem (2.31), it could only be shown that the energy is bounded by the initial energy value. Whether the energy is non increasing in time or not is still an open question.

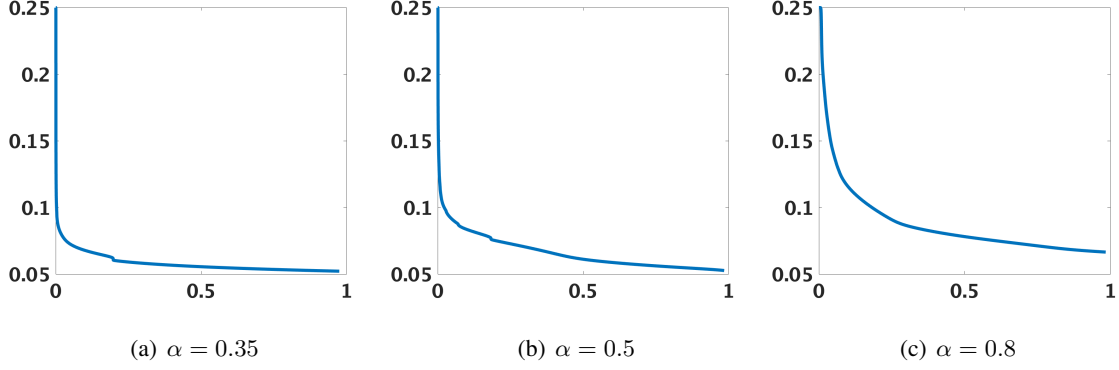


Figure 3.2: Energy evolution during the coarsening dynamics. This figures show the corresponding energies decreasing with time, with various fractional orders $\alpha = 0.35, 0.5, 0.8$.

In addition, the corresponding time step sizes used for the simulations in Figure 3.1 is also summarized in Figure 3.3. We observe that the time step size increases when the energy evolves slower. This adaptive time strategy has saved the computational resources significantly.

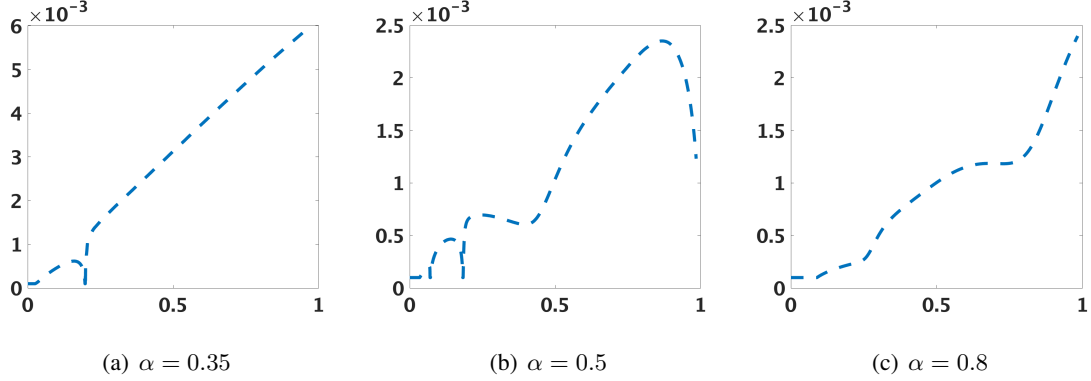


Figure 3.3: Adaptive time step sizes used during the simulation with various fractional order $\alpha = 0.35, 0.5, 0.8$.

3.3 Coarsening dynamics with various initial profiles

Next, we investigate how the initial profile would affect the coarsening dynamics. Mainly, we use the same parameters as previous subsection, i.e. $\varepsilon = 0.01$, $M = 0.1$. We set the domain $\Omega = [0, 1] \times [0, 1]$ with 128^2 meshes, and use the following initial condition

$$\phi(x, y, t = 0) = \bar{\phi}_0 + 10^{-3} \text{rand}(x, y), \quad (3.4)$$

with $rand(x, y) \in [-1, 1]$ random numbers with uniform distribution, and $\bar{\phi}_0$ a constant. Here we fix the time-fractional derivative $\alpha = 0.7$, and use different $\bar{\phi}_0$. The numerical profiles for ϕ at different times are summarized in Figure 3.4. We observe that when the volume ratio of two different components is near 1 (for instance, when $\bar{\phi}_0 = 0$), the driving mechanism for phase separation is spinodal decomposition; when the volume ratio of two different components is away from 1, the driving mechanism for phase separation is nucleation. These phenomena are with a strong agreement with the phenomena for the integer Cahn-Hilliard equation. Also, for the nucleation dynamics, the component with less volume fraction will form droplets.

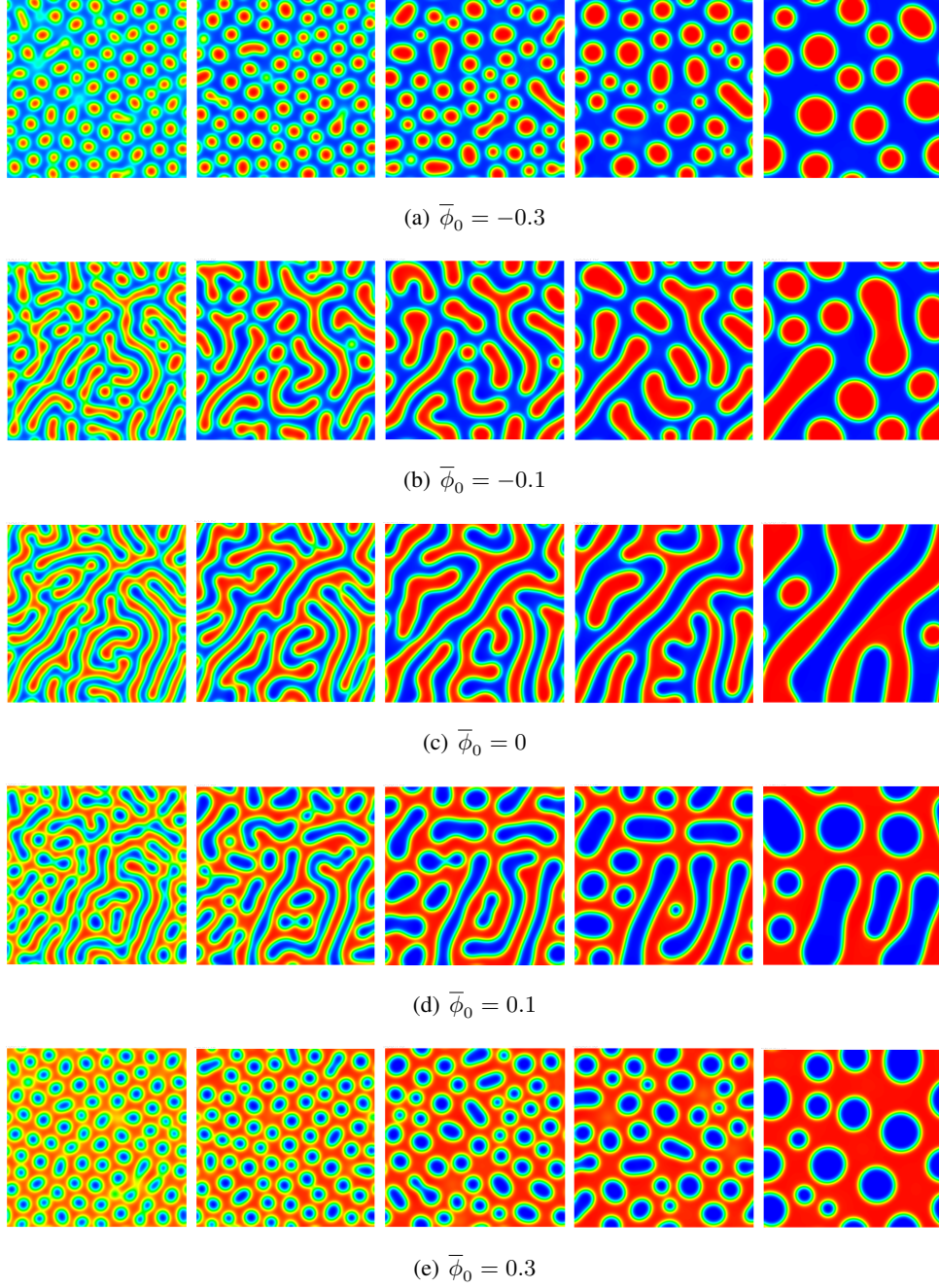


Figure 3.4: Comparison of coarsening dynamics with different initial profiles. Here we choose $\bar{\phi}_0 = -0.3, -0.1, 0, 0.1, 0.3$ and $\alpha = 0.7$ respectively. The profile of ϕ at various time slots are plotted. Here red color represents $\phi = 1$, and blue color represents $\phi = -1$.

Next, we study a more complicated case, where the initial averaged concentration varies in space. In

specific, we consider the domain $\Omega = [0, 2] \times [0, 1]$, and use the the following initial profile

$$\phi(x, y, 0) = \frac{1}{2}|x - 1| + 10^{-3}rand(x, y), \quad (3.5)$$

with $rand(x, y)$ generating uniform distributed random number in between -1 and 1. We pick $t_{\max} = 10^{-2}$, and $t_{\min} = 10^{-5}$. The numerical results with different time fractional α are summarized in Figure 3.5. We observe that near the middle part of the domain, spinodal decomposition dominates (as the volume fraction ratio is near 1); near both sides of the domain, nucleation dominates, as the one component has more volumes than the other. Also, the one with smaller fractional order α turns to have faster dynamics than those with larger fractional order α .

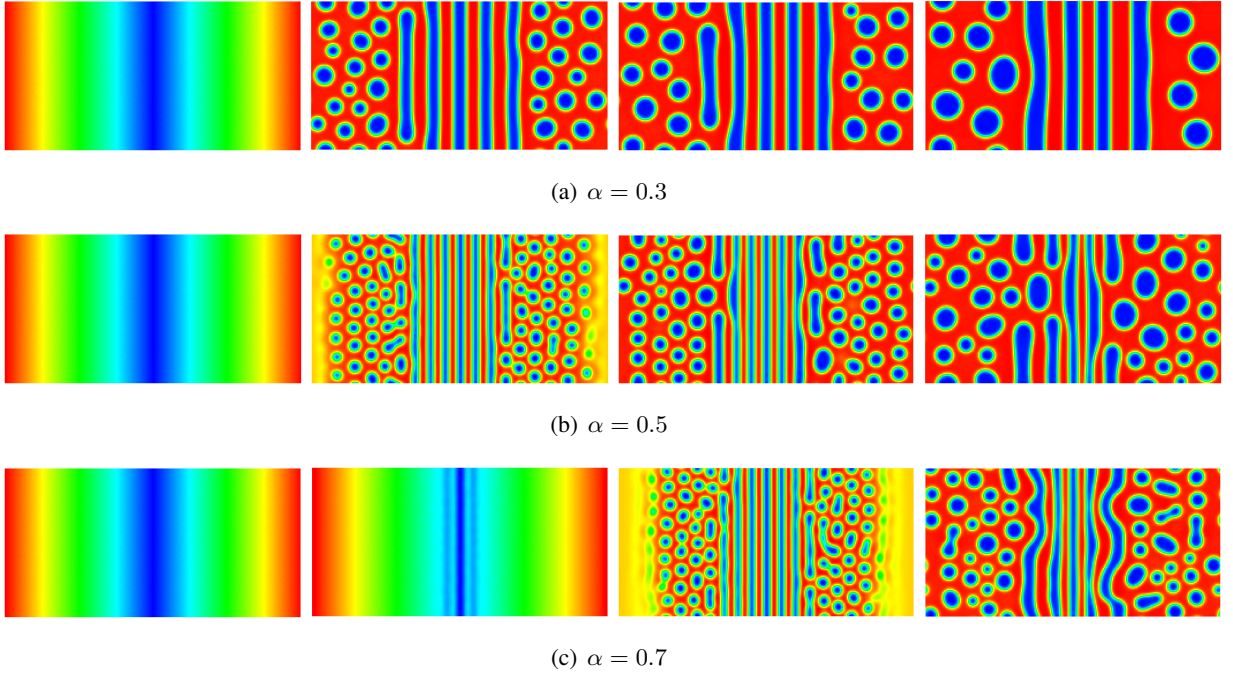


Figure 3.5: Phase separation dynamics with different fractional order parameter α and an initial condition with spatially dependent average volume fraction ratio. Here the profiles of ϕ at different time slots are shown, where (a-c) represents the cases with fractional order $\alpha = 0.3, 0.5$ and 0.7 , respectively.

3.4 Dynamics of thin-film rupture during phase separation

In this subsection, we investigate the dynamics of thin-film rupture during phase separation. We follow a similar setup as in [46]. The same model parameters are used as the previous example. Here we set the

domain $\Omega = [0, 2] \times [0, 1]$, with 256×128 uniform meshes. The initial profile for ϕ is set as

$$\phi(\mathbf{x}, 0) = \begin{cases} 0.001rand(-1, 1), & \text{if } |x - \frac{5L_x}{6} + \frac{r_0}{2} \sin(10\pi y)| < r_0, \\ -0.1 + 0.001rand(-1, 1), & \text{if } |x - \frac{3L_x}{6} + \frac{r_0}{2} \sin(10\pi y)| < r_0, \\ -0.2 + 0.001rand(-1, 1), & \text{if } |x - \frac{L_x}{6} + \frac{r_0}{2} \sin(10\pi y)| < r_0, \\ -1, & \text{other wise.} \end{cases} \quad (3.6)$$

where $r_0 = 0.05$. The numerical results for ϕ at various times are shown in Figure 3.6. We observe that different initial concentrations of liquid thin film show different rupture dynamics, where a spinodal-decomposition driven rupture pattern is observed on the right side, and a nucleation driven rupture pattern is observed on the left side.

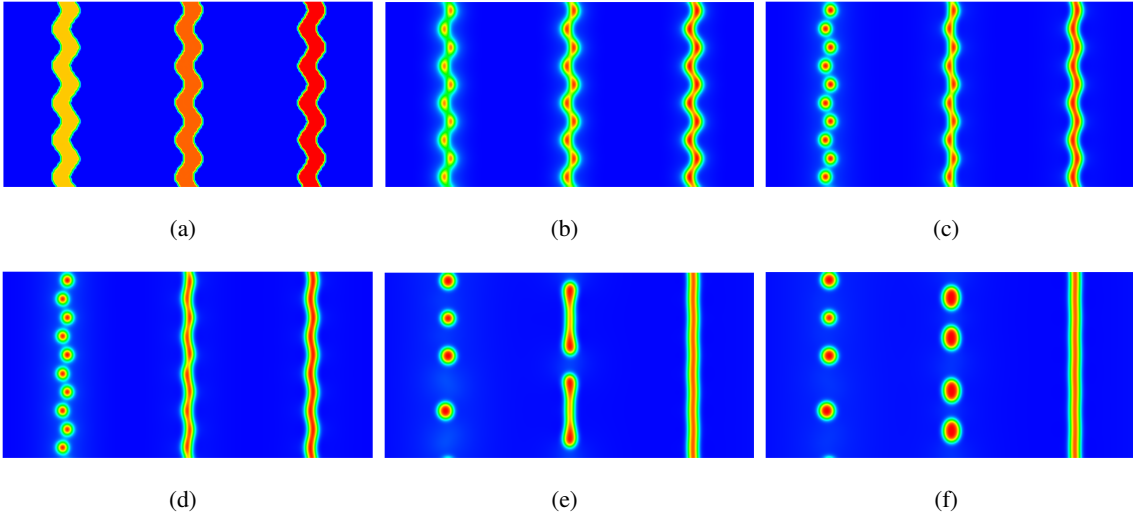


Figure 3.6: Rupture dynamics of liquid thin-film during phase separation of a binary fluid mixture. Here three thin-film columns (fluid mixture with different volume fraction ratio) are placed in a pure component. Different dynamics are observed due to the volume fraction ratio (nucleation dynamics on the left side, and spinodal dynamics on the right side). The profiles of ϕ at various time slots are shown.

In addition, the energy evolution with time is summarized in Figure 3.7(a), where we observe the energy is decreasing in time. Also, the time step size at different times is summarized in Figure 3.7(b), where we observe a relatively large time step is used at the stages when energy is decreasing slowly. This saves the computational time noticeably.

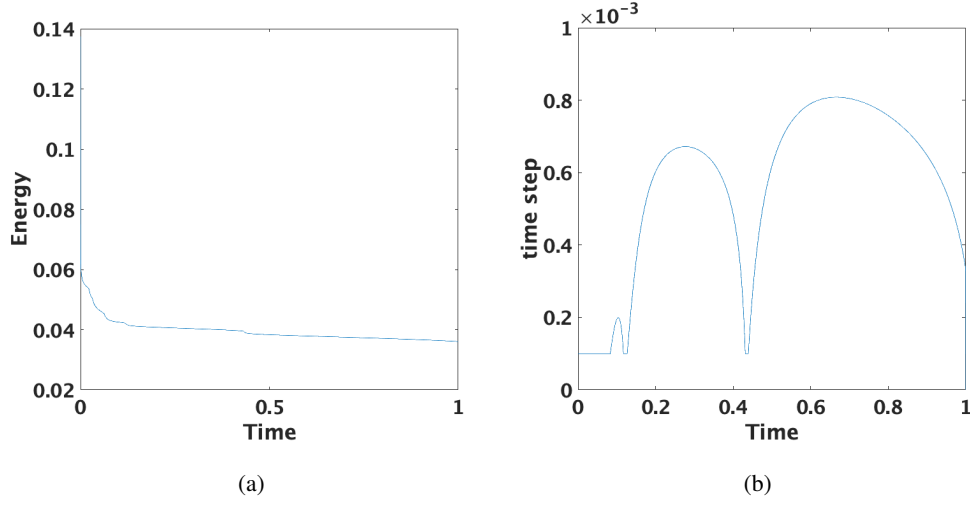


Figure 3.7: Energy evolution and time step sizes. In this figure, the energy evolution for the simulation in Figure 3.6 is shown in (a); and the adaptive time step sizes used for the simulation in Figure 3.6 is shown in (b).

Also, to numerically verify the theorem results of (2.28), we generate the graph showing the error of the total mass, i.e., the difference of

$$\int_{\Omega} \phi(\mathbf{x}, t) d\mathbf{x} - \int_{\Omega} \phi(\mathbf{x}, 0) d\mathbf{x},$$

which is summarized in Figure 3.8. We observe that the difference is in the order of $O(10^{-14})$, which is negligible. This is in strong agreement with (2.28), i.e., our proposed numerical algorithm preserves the total mass of the phase variable ϕ .

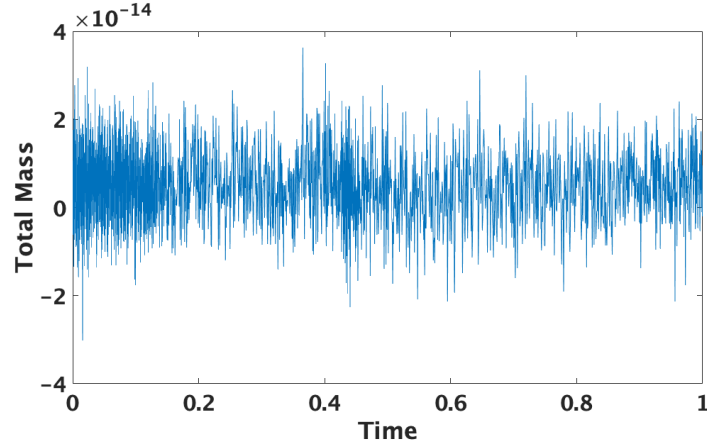


Figure 3.8: Time evolution of the total volume error for the phase variable ϕ . This figure shows the time evolution of $\int_{\Omega} \phi(\mathbf{x}, t) d\mathbf{x} - \int_{\Omega} \phi(\mathbf{x}, 0) d\mathbf{x}$.

4 Conclusion

In this paper, we propose a new algorithm for solving the time-fractional Cahn-Hilliard equation. The resulted numerical scheme has several advantages. It allows non-uniform time step, such that adaptive time step sizes could be utilized to save computational time. It is unconditionally energy stable, assuring the stability of the numerical algorithm. The existence and uniqueness of the numerical solution are also verified theoretically. Several numerical tests are shown to confirm these advantages.

Acknowledgments

The work of Jun Zhang is supported by the National Natural Science Foundation of China (No. 11901132), the China Scholarship Council (No. 201908525061) and the Science and Technology Program of Guizhou Province (No.[2020]1Y013). Jia Zhao would like to acknowledge the support by National Science Foundation, USA, with grant number DMS-1816783.

References

- [1] J. F. Blowey and C. M. Elliott. The Cahn–Hilliard gradient theory for phase separation with non-smooth free energy part I: Mathematical analysis. *European Journal of Applied Mathematics*, 2(3):233–280, 1991.

- [2] J. F. Blowey and C. M. Elliott. The Cahn–Hilliard gradient theory for phase separation with non-smooth free energy part II: Numerical analysis. *European Journal of Applied Mathematics*, 3(2):147–179, 1992.
- [3] F. Guillen-Gonzalez and G. Tierra. On linear schemes for a Cahn–Hilliard diffuse interface model. *Journal of Computational Physics*, 234:140–171, 2013.
- [4] F. Guillen-Gonzalez and G. Tierra. Second order schemes and time-step adaptivity for Allen–Cahn and Cahn–Hilliard models. *Computers and Mathematics with Applications*, 68(8):821–846, 2014.
- [5] Y. Li, H. Lee, and B. Xia and J. Kim. A compact fourth-order finite difference scheme for the three-dimensional Cahn–Hilliard equation. *Computer Physics Communications*, 200:108–116, 2016.
- [6] Z. Guan, J. Lowengrub, C. Wang, and S. Wise. Second order convex splitting schemes for periodic nonlocal Cahn–Hilliard and Allen–Cahn equations. *Journal of Computational Physics*, 227:48–71, 2014.
- [7] H. Jia, Y. Guo, J. Li, and Y. Huang. Analysis of a novel finite element method for a modified cahn-hilliard-hele-shaw system. *Journal of computational and applied mathematics*, 376(112846):1–13, 2020.
- [8] C. M. Elliott and A. M. Stuart. The global dynamics of discrete semilinear parabolic equations. *SIAM Journal on Numerical Analysis*, 30(6):1622–1663, 1993.
- [9] D. Eyre. Unconditionally gradient stable time marching the Cahn–Hilliard equation. *Computational and mathematical models of microstructural evolution (San Francisco, CA, 1998)*, 529:39–46, 1998.
- [10] Z. Hu, S. M. Wise, C. Wang, and J. S. Lowengrub. Stable and efficient finite-difference nonlinear-multigrid schemes for the phase field crystal equation. *Journal of Computational Physics*, 228(15):5323–5339, 2009.
- [11] J. Zhu, L. Q. Chen, J. Shen, and V. Tikare. Coarsening kinetics from a variable-mobility Cahn–Hilliard equation: Application of a semi-implicit fourier spectral method. *Physical Review E*, 60(4):3564, 1999.
- [12] J. Zhao, X. Yang, Y. Gong, and Q. Wang. A novel linear second order unconditionally energy stable scheme for a hydrodynamic \mathbf{Q} -tensor model of liquid crystals. *Computer Methods in Applied Mechanics and Engineering*, 318:803–825, 2017.

- [13] X. Yang, J. Zhao, and Q. Wang. Numerical approximations for the molecular beam epitaxial growth model based on the invariant energy quadratization method. *Journal of Computational Physics*, 333:104–127, 2017.
- [14] J. Shen, J. Xu, and J. Yang. The scalar auxiliary variable (SAV) approach for gradient flows. *Journal of Computational Physics*, 353:407–416, 2018.
- [15] Z. Z. Sun. A second-order accurate linearized difference scheme for the two-dimensional Cahn–Hilliard equation. *Numerische Mathematik*, 64(212):1463–1471, 1995.
- [16] Y. Yan, W. Chen, C. Wang, and S. Wise. A second-order energy stable BDF numerical scheme for the Cahn–Hilliard equation. *Numerische Mathematik*, 23(2):572–602, 2018.
- [17] K. Cheng, C. Wang, S. M. Wise, and X. Yue. A second-order, weakly energy-stable pseudo–spectral scheme for the Cahn–Hilliard equation and its solution by the homogeneous linear iteration method. *Journal of Scientific Computing*, 69(3):1083–1114, 2016.
- [18] X. Feng and A. Prohl. Error analysis of a mixed finite element method for the Cahn–Hilliard equation. *Numerische Mathematik*, 99(1):47–84, 2004.
- [19] A. E. Diegel, C. Wang, and S. M. Wise. Stability and convergence of a second-order mixed finite element method for the Cahn–Hilliard equation. *IMA Journal of Numerical Analysis*, 36(4):1867–1897, 2016.
- [20] S. Wise, C. Wang, and J. S. Lowengrub. An energy-stable and convergent finite-difference scheme for the phase field crystal equation. *SIAM Journal of Numerical Analysis*, 47(3):2269–2288, 2009.
- [21] C. Wang and S. M. Wise. An energy stable and convergent finite-difference scheme for the modified phase field crystal equation. *SIAM Journal on Numerical Analysis*, 49(3):945–969, 2011.
- [22] A. Baskaran, J. S. Lowengrub, C. Wang, and S. Wise. Convergence analysis of a second order convex splitting scheme for the modified phase field crystal equation. *SIAM Journal on Numerical Analysis*, 51(5):2851–2873, 2013.
- [23] J. Shen, C. Wang, X. Wang, and S. M. Wise. Second-order convex splitting schemes for gradient flows with Ehrlich–Schwoebel type energy: application to thin film epitaxy. *SIAM Journal on Numerical Analysis*, 51(1):105–125, 2012.
- [24] Z. Guan, C. Wang, and S. M. Wise. A convergent convex splitting scheme for the periodic nonlocal Cahn–Hilliard equation. *Numerische Mathematik*, 128(2):377–406, 2014.

- [25] W. Chen, Y. Liu, C. Wang, and S. Wise. Convergence analysis of a fully discrete finite difference scheme for the Cahn–Hilliard–Hele–Shaw equation. *Mathematics of Computation*, 85(301):2231–2257, 2016.
- [26] D. Han and X. Wang. A second order in time, uniquely solvable, unconditionally stable numerical scheme for Cahn–Hilliard–Navier–Stokes equation. *Journal of Computational Physics*, 290:139–156, 2015.
- [27] M. Ainsworth and Z. Mao. Analysis and approximation of a fractional Cahn–Hilliard equation. *SIAM Journal on Numerical Analysis*, 55(4):1689–1718, 2017.
- [28] M. Ainsworth and Z. Mao. Well-posedness of the Cahn–Hilliard equation with fractional free energy and its Fourier Galerkin approximation. *Chaos, Solitons and Fractals*, 102:264–273, 2017.
- [29] H. Liu, A. Cheng, H. Wang, and J. Zhao. Time-fractional Allen–Cahn and Cahn–Hilliard phase-field models and their numerical investigation. *Computers and Mathematics with Applications*, 76(8):1876–1892, 2018.
- [30] Q. Du, J. Yang, and Z. Zhou. Time-fractional Allen–Cahn equations: Analysis and numerical methods. *arXiv preprint arXiv:1906.06584*, 2019.
- [31] T. Tang, H. Yu, and T. Zhou. On energy dissipation theory and numerical stability for time-fractional phase field equations. *arXiv preprint arXiv:1808.01471*, 2018.
- [32] J. Zhao, L. Chen, and H. Wang. On power law scaling dynamics for time-fractional phase field models during coarsening. *Communications in Nonlinear Science and Numerical Simulation*, 70:257–270, 2019.
- [33] L. Chen, J. Zhang, J. Zhao, W. Cao, H. Wang, and J. Zhang. An accurate and efficient algorithm for the time-fractional molecular beam epitaxy model with slope selection. *Computer Physics Communications*, 245:106842, 2019.
- [34] Y. Lin and C. Xu. Finite difference/spectral approximations for the time-fractional diffusion equation. *Journal of computational physics*, 225(2):1533–1552, 2007.
- [35] S. Dai and Q. Du. Computational studies of coarsening rates for the Cahn–Hilliard equation with phase-dependent diffusion mobility. *Journal of Computational Physics*, 310:85–108, 2016.

- [36] B. Ji, H. L. Liao, Y. Gong, and L. Zhang. Adaptive second-order Crank–Nicolson time-stepping schemes for time fractional molecular beam epitaxial growth models. *arXiv preprint arXiv:1906.11737*, 2019.
- [37] B. Ji, H. Liao, Y. Gong, and L. Zhang. Adaptive linear second-order energy stable schemes for time-fractional Allen–Cahn equation with volume constraint. *arXiv*, page 11909.1093, 2019.
- [38] Z. Zhang and Z. Qiao. An adaptive time-stepping strategy for the Cahn–Hilliard equation. *Communications in Computational Physics*, 11(4):1261–1278, 2012.
- [39] B. Jin, R. Lazarov, and Z. Zhou. An analysis of the l_1 scheme for the subdiffusion equation with nonsmooth data. *IMA Journal of Numerical Analysis*, 36(1):197–221, 2015.
- [40] H. L. Liao, D. Li, and J. Zhang. Sharp error estimate of the nonuniform l_1 formula for linear reaction-subdiffusion equations. *SIAM Journal on Numerical Analysis*, 56(2):1112–1133, 2018.
- [41] H. L. Liao, Y. Yan, and J. Zhang. Unconditional convergence of a fast two-level linearized algorithm for semilinear subdiffusion equations. *Journal of Scientific Computing*, pages 1–25, 2019.
- [42] W. McLean, V. Thomée, and L. B. Wahlbin. Discretization with variable time steps of an evolution equation with a positive-type memory term. *Journal of computational and applied mathematics*, 69(1):49–69, 1996.
- [43] W. McLean and K. Mustapha. A second-order accurate numerical method for a fractional wave equation. *Numerische Mathematik*, 105(3):481–510, 2007.
- [44] L. Chen, J. Zhao, and Y. Gong. A novel second-order scheme for the molecular beam epitaxy model with slope selection. *Commun. Comput. Phys*, x(x):1–21, 2019.
- [45] Y. Gong, J. Zhao, and Q. Wang. Linear second order in time energy stable schemes for hydrodynamic models of binary mixtures based on a spatially pseudospectral approximation. *Advances in Computational Mathematics*, 44:1573–1600, 2018.
- [46] H. Gomez, A. Reali, and G. Sangalli. Accurate efficient and isogeometrically flexible collocation methods for phase field models. *Journal of Computational Physics*, 262:153–171, 2014.